GEM - International Journal on Geomathematics (2025) 16:2
https://doi.org/10.1007/s13137-024-00260-1

ORIGINAL PAPER

Kalman filter framework for a regional mass change model from GRACE satellite gravity

Viviana Wöhnke[1] · Annette Eicker[1] · Matthias Weigelt[2,3] · Marvin Reich[4] · Andreas Güntner[4,5] · Andreas Kvas[6] · Torsten Mayer-Gürr[7]

Received: 22 December 2023 / Accepted: 28 November 2024 / Published online: 9 December 2024

Abstract
In this study a regional modelling framework for water mass changes is developed. The approach can introduce geodetic observation types of varying temporal and spatial resolution including their correlated error information. For this purpose a Kalman filter process was set up using a regional parameterisation by space-localising radial basis functions and a process model based on stochastic prediction. The feasibility of the approach is confirmed in a closed-loop simulation experiment using gridded water storage estimates derived from simulated monthly solutions of the GRACE satellite gravimetry mission and considering realistic error patterns. The resulting mass change time series exhibit strongly reduced noise and a very high agreement with the reference model. The modelling framework is designed to flexibly allow a future extension towards combining satellite gravimetry with other geodetic observations such as GNSS station displacements or terrestrial gravimetry.

Keywords Regional gravity field modelling · Radial basis functions · Kalman filter · Terrestrial water storage · GRACE · Satellite gravimetry

Mathematics Subject Classification 86A30 · 60G35

1 Introduction

Geodetic measurements play a crucial role in understanding the Earth's structure and dynamics and are sensitive to changes in water mass on and below the Earth's surface. For water resources management, for understanding the impacts of climate change and human water use on the water cycle, and for an early preparedness to drought and flood hazards, the regional monitoring of water storage, i.e. water mass changes with high temporal and spatial resolution, is of crucial importance but currently not available. Various geodetic techniques are able to observe mass changes in the Earth system: a) satellite gravimetry, b) terrestrial absolute and relative gravimetry, and c) GNSS and InSAR by observing vertical displacements. In addition, networks of optical clocks are in development and are approaching the level of 10^{-18} equivalent to a precision

Extended author information available on the last page of the article

of 1 cm in geoid height. According to the general relativity theory, a change in the frequency of optical clocks can be related to a change in the gravitational potential, which again depends on the mass distribution. The principle is described, for example in Lisdat et al. (2016) and Müller et al. (2018). Ideally, all observation types are combined in a uniform modelling framework to exploit their individual advantages and limitations in terms of sensitivity, availability, and spatial and temporal resolution with the goal to enable the unprecedented ability to describe water storage changes from the landscape to river basin scales with a higher than monthly temporal resolution. Such a modelling framework should (1) be able to incorporate various observation types with different temporal and spatial resolutions, (2) allow the introduction of complex error information, and (3) be based on a flexible regional parameterisation.

Space-borne gravity missions like the Gravity Recovery and Climate Experiment (GRACE, Tapley et al. 2004) and GRACE-FO (Follow-On, Landerer et al. 2020) are able to provide global information on variations in continental water storage (Tapley et al. 2019) with a footprint of 200 km – 300 km and a relatively low temporal resolution (typically 1 month), and are therefore often too coarse to deliver information at the scale of individual aquifers or river catchments that are relevant for water management applications. Terrestrial gravimetry is primarily sensitive to local redistribution of water mass at the metre to kilometre scale and their respective mass changes, and can be available at sub-daily resolution (Güntner et al. 2017). Global Navigation Satellite System (GNSS) site displacements capture the elastic response of the Earth to changes in water storage, providing insight into global to regional-scale mass variations typically on a daily basis (Argus et al. 2014). These three geodetic techniques therefore complement each other in terms of spatial and temporal resolutions but also come with their system-specific error behaviour. To ensure a proper relative weighting of the three observation types when combining them into an integrative data set of water storage variations, the estimation framework needs to consider the available error information. In particular, the GRACE/-FO data are characterised by complex and spatially highly correlated error patterns (Swenson and Wahr 2006) that need to be incorporated into the parameter estimation process in terms of full variance-covariance matrices.

The optimal exploitation of the signal content of geodetic observations in a region of interest requires a regional gravity field (or mass change) modelling. Gravity field models derived from the GRACE/-FO missions are most commonly parameterised in terms of Stokes coefficients, which are the dimensionless spherical harmonic coefficients of the geopotential (Heiskanen and Moritz 1967; Wahr et al. 1998) with the disadvantage that regional characteristics cannot be properly represented by basis functions with global support (Eicker 2008). Such a representation with a high spatial and a globally uniform resolution results in a large number of parameters to be used to recover the regional water mass signal and often related instabilities during the estimation process. A more suitable alternative for modelling of regional mass change represent parameterisations based on space-localising basis functions. The so-called mascon approach (Rowlands et al. 2005) uses regional mass concentration blocks and has become a popular alternative over recent years but has in the context of GRACE/-FO data processing mainly been used for the estimation of global gravity field models (Watkins et al. 2015; Loomis et al. 2019; Save et al. 2016). Mascon models were also estimated from global spherical harmonic representations, e.g. for Greenland, to mit-

igate spatial leakage effects (Schrama et al. 2014; Ran et al. 2018). Regional gravity models based on spherical radial basis functions (RBF) as introduced by Freeden and Törnig (1981) have been derived by Bentel et al. (2013), Eicker et al. (2014), and Liu et al. (2020), but focus on the static mean gravity field. Only few studies have dealt with the estimation of temporal gravity field variations by making use of a regional representation. An early study by Schmidt et al. (2006) used multi-resolution RBFs, in which a wavelet-type representation provides signal approximations at different resolution levels, for the determination of mass change in South America from GRACE. Spatio-spectrally localising Slepian functions were applied to detect the gravity signal caused by the Andaman earthquake from GRACE data (Han and Simons 2008) and to the mapping of ice mass variations (Harig and Simons 2012; von Hippel and Harig 2019). Recently, Ramillien et al. (2020) successfully determined regional surface water mass using a set of triangular surfaces of constant area for the parameterisation and Ramillien et al. (2021) successfully estimated high-resolution water mass changes in Africa directly from GRACE inter-satellite K-band (level 1B) data using Slepians. Despite these promising examples, the use of regional modelling to mass change estimation from satellite gravimetry is still comparably rare and not being processed on an operational basis.

A parameter estimation method well suited for the representation of time-variable quantities is the Kalman filter algorithm (Kalman 1960). It has successfully been implemented for the estimation of global daily GRACE gravity field models from level 1B data, see Kurtenbach et al. (2012) and Kvas et al. (2019). In the present study, the Kalman filter approach shall be tailored to the estimation of regional water mass change for a test region in central Europe, with a regional parameterisation based on RBFs as described in Eicker (2008) and Eicker et al. (2014). In a closed-loop simulation scenario based on gridded GRACE data, the feasibility and stability of the approach is assessed and its ability to represent regional temporal water storage variations is demonstrated. The Kalman filter allows the introduction of other observation types such as terrestrial gravimetry and GNSS into the estimation procedure at a later stage.

The paper is organised as follows: After this introduction (Sect. 1), the following Sect. 2 describes the simulated data sets including the generation of realistic correlated errors. In the following Sect. 3, the regional parameterisation by space-localising RBFs is introduced and the shape and location of the RBFs is discussed. Section 4 describes the general setting of the Kalman filter framework including detailed information on the process model that is chosen to predict (water) mass change from one time step to the next. The results of the simulation experiment are presented in Sect. 5. Section 6 summarises the main findings of the study and indicates future developments towards a combination of various geodetic data sets in the developed estimation framework.

2 Simulated data sets and uncertainties

The Kalman filter is set up in a closed-loop simulation environment, i.e. in a controlled setting with observations simulated from a known reference model, in which different configurations, settings, point distributions and other variables can be tested. Hence, in the study presented here no real data are applied, but the European Space Agency

(ESA) Earth System Model (ESA ESM, Dobslaw et al. 2015) is used to generate time series that serve as simulated observations in the Kalman filter. The ESA ESM is a synthetic model for satellite gravity mission simulation studies that contains global mass variability including a seasonal signal, year-to-year variability and multi-year trends. The data are provided as spherical harmonic coefficients up to degree and order 180 (corresponding to an approximate spatial resolution of 111 km) and cover the time period from 1995 to 2006 with a resolution of 6 h.

In this study, a Kalman filter is set up that contains only simulated GRACE data and thus only one type of (pseudo) observations. Other observation types like e.g. GNSS loading and terrestrial gravimetry will be incorporated into the simulation environment at a later stage. The test area used in this study is located in central Europe and covers most of the inland area between France, Poland and Hungary as can be seen in a figure shown later in the paper (see Fig. 4) denoted by $\partial\Omega_I$ in black.

In order to simulate GRACE observations from the ESA ESM model data, the data are processed to exhibit realistic properties very similar to (post-processed) real GRACE data. This approach is based on the data processing used by Kvas (2020) where residual time series $\tilde{\mathbf{v}}_i$ are computed, which consist of the residual ESA ESM components H (hydrology), I (land ice) and AOerr (atmosphere and ocean errors). The latter takes into account that the largest part of the atmospheric and oceanic mass variations are already subtracted during the GRACE level 1B processing in the so-called de-aliasing procedure. Using the Gravity Recovery Object Oriented Programming System (GROOPS, Mayer-Gürr et al. 2021), the data are first downsampled to the targeted resolution of one month, i.e. monthly averages are calculated from the ESA ESM data. In order to obtain the residuals of the individual components, the time series are reduced by its mean, linear trend, annual and semi-annual signal, and then summed to yield the following residual time series:

$$\tilde{\mathbf{v}}_i = \tilde{\mathbf{v}}_i^{\mathrm{H}} + \tilde{\mathbf{v}}_i^{\mathrm{I}} + \tilde{\mathbf{v}}_i^{\mathrm{AOerr}}. \tag{1}$$

To match the spectral content of real GRACE solutions, the time series are first truncated to spherical harmonic coefficients of degrees $2-96$ and smoothed with a 300 km Gaussian filter. The data are then limited to the test area in central Europe by converting from spherical harmonics to gridded data in the observation area $\partial\Omega_O$ on a 1° geographic grid. In Fig. 4, the observation grid (orange) is plotted together with the locations of the RBFs. To account for the characteristic noise pattern of GRACE, realistic noise with stochastic properties from the covariance matrix of one GRACE month (2008-01) processed by the Institute of Geodesy, Working Group Theoretical Geodesy and Satellite Geodesy (ITSG) at Graz University of Technology (Mayer-Gürr et al. 2018) is added to the ESA ESM residual time series. There is a very good agreement between empirical noise estimates and the formal covariance matrices of ITSG-Grace products, which has been shown in previous studies (Kvas et al. 2019; Kvas and Mayer-Gürr 2019), especially when compared to other publicly available covariance information. While not perfect, this matrix is a realistic estimate of the GRACE post-fit errors and the result of an immense effort to model stationary and non-stationary observation noise (Ellmer 2018; Kvas et al. 2019). This observational noise model is derived in an iterative process by performing postfit residual analysis for

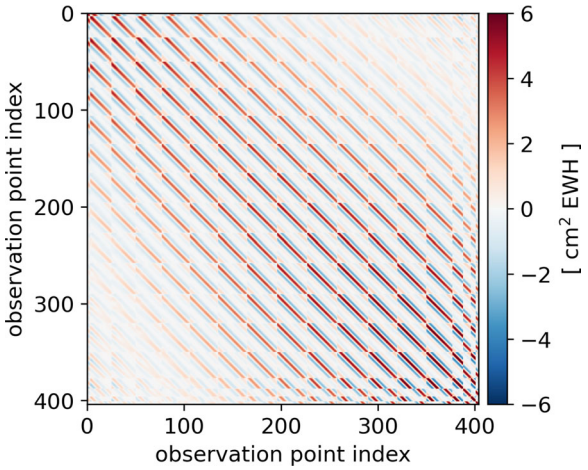

Fig. 1 300 km Gaussian-filtered GRACE covariance matrix (2008-01), propagated to gridded values in the observation area $\partial\Omega_O$

both types of GRACE observations (inter-satellite range rates and kinematic orbits). Additionally, the errors of the background models (the so-called de-aliasing models) are introduced into the estimation process (Kvas and Mayer-Gürr 2019). Modelling these two error sources covers the current main contributors to derived gravity field solutions (Flechtner et al. 2016) and thus provide a realistic, close approximation of the actual uncertainties. It is therefore assumed that the covariance matrix used to derive our synthetic noise model is indeed a realistic representation of the real GRACE errors.

As we use filtered time series, the same 300 km Gaussian filter is also applied to the GRACE covariance matrix of the exemplary month. The matrix is then propagated to gridded values covering the observation area $\partial\Omega_O$ with the same spatial sampling of 1° like the residual ESA ESM time series $\tilde{\mathbf{v}}$. The resulting covariance matrix of the gridded values is shown in Fig. 1. The striped structure of the covariance matrix results from the noise pattern of GRACE and from the sorting and assignment of indices to the grid points in the observation area.

The generation of GRACE-like noise can be seen as a transformation from uncorrelated variables $\bar{\mathbf{l}}$ with covariance matrix $\mathcal{C}(\bar{\mathbf{l}}) = \sigma_0^2\mathbf{I}$ to a set of correlated variables $\mathbf{l}$ with $\mathcal{C}(\mathbf{l}) = \sigma_0^2\boldsymbol{\Sigma}$. If $\boldsymbol{\Sigma}$ contains the targeted variances and covariances and is positive-definite, the Cholesky decomposition can be used to decompose $\boldsymbol{\Sigma}$ into the product of an upper triangular matrix $\mathbf{W}$, which is the Cholesky matrix, and its conjugate transpose $\mathbf{W}^T$:

$$\boldsymbol{\Sigma} = \mathbf{W}^T\mathbf{W}. \tag{2}$$

The lower triangular matrix $\mathbf{W}^T$ can then be used to transform the uncorrelated, standard-normal noise $\bar{\mathbf{l}}$ into correlated noise $\mathbf{l}$:

$$\mathbf{l} = \mathbf{W}^T\bar{\mathbf{l}} \tag{3}$$

(Koch 1999; Mayer-Gürr 2006). With the Gaussian-filtered GRACE covariance matrix $\boldsymbol{\Sigma}$ containing the variances and covariances, from which $\mathbf{W}^T$ can be calculated, the

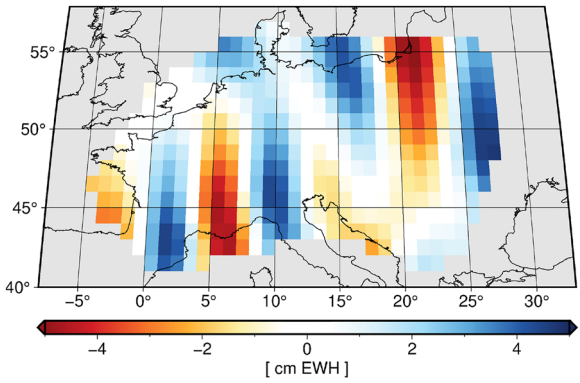

Fig. 2 Example of correlated GRACE-like noise for one exemplary month (2006-02)

insertion into Eq. 3 gives the GRACE-like correlated noise, which is different for each time step, with the exemplary noise for one time step being shown in Fig. 2. To account for the non positive-definite characteristic of the gridded GRACE covariance matrix, $\mathbf{\Sigma}$ is replaced by $\mathbf{\Sigma} + \kappa\mathbf{I}$, i.e. $\mathbf{\Sigma}$ is regularised by adding a small value $\kappa = 10^{-12}$ to the main diagonal that is sufficient to make $\mathbf{\Sigma}$ invertible without applying a too strong regularisation.

The correlated noise is added to the ESA ESM residual time series $\tilde{\mathbf{v}}$:

$$\tilde{\mathbf{v}}_{\text{noise}} = \tilde{\mathbf{v}} + \text{chol}\,(\mathbf{\Sigma} + \kappa\mathbf{I})^T\,\bar{\mathbf{l}} \tag{4}$$

which results in the noisy simulated observation time series that is used as input for the Kalman filter. The Gaussian-filtered time series without added noise yields an area-weighted mean temporal RMS (i.e. for all time steps and grid cells in the observation area $\partial\Omega_O$) of 3.03 cm equivalent water height (EWH), while the noisy simulated observation time series $\tilde{\mathbf{v}}_{\text{noise}}$ has an RMS of 3.78 cm EWH in the observation area.

3 Parameterisation

The global spherical harmonic basis functions (Heiskanen and Moritz 1967; Wahr et al. 1998) are not well suited to represent local or regional mass changes like aimed at in this study. Spherical harmonics are global by nature and correlated in space, thus changes in one coefficient affect the whole sphere and changes occurring in a spatially bounded area result in a change of all spherical harmonic coefficients, making the modelling of a time-variable gravity field computationally expensive. Therefore, an alternative regional modelling approach has been developed based on space-localising RBFs (Eicker 2008; Eicker et al. 2014) which effectively differ from zero only in a spatially limited area and can therefore be regarded as space-localising. The idea of regional modelling is to define RBFs with a specific shape at a given grid of locations and then to multiply each RBF with a scaling coefficient to represent the signal of interest. These coefficients have a similar role as the Stokes coefficients in a spherical

harmonic expansion, but they do not each refer to a specific frequency, but to a specific RBF at a given location. The scaling coefficients serve as unknown parameters in the Kalman filter framework.

As RBFs are radially symmetric, they depend only on the spherical distance between the nodal grid point $\mathbf{x}_k$ at which the radial basis function is located and the evaluation grid point $\mathbf{x}$, both of which lie on the unit sphere Ω with $\Omega = \{\mathbf{x} \in \mathbb{R}^3 \mid |\mathbf{x}| = 1\}$. A functional s at the location $\mathbf{x}$ can be modelled as a sum of K RBFs $\Phi_k(\mathbf{x}, \mathbf{x}_k)$ placed globally or in a spatially bounded region, with each basis function being multiplied by an individual scaling coefficient a_k according to

$$\mathrm{s}(\mathbf{x}) = \sum_{k=1}^{K} \mathrm{a}_k \Phi_k(\mathbf{x}, \mathbf{x}_k). \tag{5}$$

The properties to be specified when defining an RBF parameterisation are the shape of the Φ_k and their locations $\mathbf{x}_k$. To define the former, the radially symmetric RBFs can be expressed as a series expansion of Legendre polynomials P_n with each Legendre polynomial being multiplied by a shape coefficient φ_n. The basis functions $\Phi_k(\mathbf{x}, \mathbf{x}_k)$ including the conversion to EWH up to a maximum degree N are then computed according to

$$\Phi_k(\mathbf{x}, \mathbf{x}_k) = \sum_{n=2}^{N} \sqrt{2n+1} \cdot \varphi_n \mathrm{P}_n(\mathbf{x} \cdot \mathbf{x}_k) \left(\frac{\mathrm{R}}{\mathrm{r}}\right)^{n+1} \frac{2n+1}{4\pi \mathrm{G}\rho \mathrm{r}} \frac{1}{1+\mathrm{k}_n'} \tag{6}$$

with the fully normalised Legendre polynomials P_n and the radii R (nodal grid points $\mathbf{x}_k$) and r (evaluation grid points $\mathbf{x}$). The last part of the equation $\frac{2n+1}{4\pi \mathrm{G}\rho \mathrm{r}} \frac{1}{1+\mathrm{k}_n'}$ is needed for the conversion from gravitational potential to EWH (Wahr et al. 1998). Here ρ denotes the water density, G the gravitational constant, and k_n' the load Love deformation numbers (Farrell 1972, numerical values were calculated by Pascal Gegout, provided by Jean-Paul Boy and downloaded from http://astrogeo.org/agra/Load_Love2_CM.dat). The φ_n, which are assumed to be identical for all Φ_k, are the coefficients that define the shape of the basis functions.

The rationale behind the specific basis functions used in our study follows Eicker (2008). It is based on the assumption that the Earth's gravity field possesses a certain degree of smoothness, which can be deduced from the spectral behaviour of the gravity field as defined, e.g. by the degree amplitudes σ_n of a spherical harmonic expansion. To incorporate these smoothness conditions into the shape of the basis functions, we define the shape coefficients φ_n according to

$$\varphi_n = \frac{\mathrm{GM}}{\sqrt{4\pi}\mathrm{R}} \frac{\sigma_n}{\sqrt{2n+1}}, \tag{7}$$

which implies that our basis functions follow from the frequency-domain behaviour of the expected gravity field signal. Consequences arising from this choice of the RBF kernel are detailed in Eicker (2008) and Eicker et al. (2014).

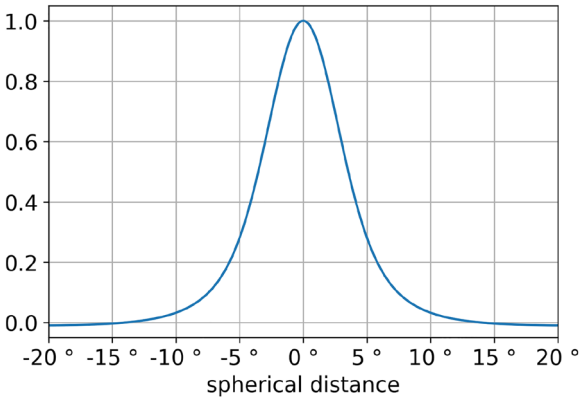

Fig. 3 Shape of the RBF for max degree n=96 with shape coefficients φ_n derived from ESA ESM residuals for all months (mean)

In our simulation study, the φ_n are derived from the 300 km Gaussian-filtered ESA ESM residual degree amplitudes σ_n by computing a set of coefficients for each month and averaging them, leading to the RBF shape shown in Fig. 3. As an alternative to computing the RBF shape coefficients φ_n from the ESA ESM model, they could also be derived from σ_n that follow Kaula's rule of thumb (Kaula 1966), which was introduced as an approximation of the spectral behaviour of the gravity field signal. As is briefly discussed in Sect. 5, this does not substantially change the Kalman filter results.

The second important property of an RBF representation is the distribution of the RBFs on the nodal grid points $\mathbf{x}_k$. The number of grid points and accordingly also the distance between the points, defines the spatial resolution of the modelled gravity field. Due to the advantages in terms of homogeneous distribution and adjustability of the number of grid points as discussed by Eicker (2008), the "triangle vertex" grid, which corresponds to the geodesic grid described by Vestine et al. (1963), is chosen for the placement of the basis functions. The spatial resolution of the grid corresponds to the global number of homogeneously distributed grid points determined by the triangle vertex level j according to

$$K = 10 \cdot (j+1)^2 + 2. \tag{8}$$

To define K, the number of parameters of a spherical harmonic expansion of the desired spatial resolution with maximum degree N is taken as reference and the minimum number of RBF scaling coefficients a_k can be computed according to $K_{\min} = (N+1)^2$. It should be noted here that the number of basis functions required refers to a global modelling and the number of basis functions is accordingly much smaller for the test area in central Europe.

In the modelling, three different areas have to be distinguished: the evaluation or investigation area $\partial\Omega_I$, where the final (water) mass changes are calculated, the area $\partial\Omega_O$ where the observations are available and the area where the RBFs are placed: the computation area $\partial\Omega_C$. The reasons for this are described, for example, by Liu et al. (2020): In the outer regions of the observation area $\partial\Omega_O$, the sought scaling coefficients a_k cannot be estimated sufficiently well due to the lack of observations

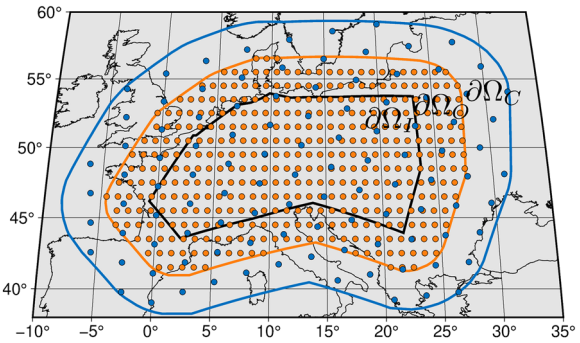

Fig. 4 Point distributions for the investigation area $\partial\Omega_I$ (1° grid, black, same point locations as orange points), observation area $\partial\Omega_O$ (1° grid, 300 km buffer wrt. $\partial\Omega_I$, orange) and computation area $\partial\Omega_C$ (triangle vertex grid of level n=30, 300 km buffer wrt. $\partial\Omega_O$, blue) (colour figure online)

beyond the boundary, resulting in edge effects. To avoid these effects in the evaluation area $\partial\Omega_I$, the observation area $\partial\Omega_O$ should be larger. Since the basis functions do not have perfect space-localising properties and oscillation effects occur especially in the edge areas, the computation area in which the RBFs are placed should be larger than the observation area $\partial\Omega_O$ and thus represent the largest of the three areas. The choice of the margins depends on the shape and placement of the RBFs, since at higher maximum degree N the RBFs become narrower and at the same time more RBFs are placed (see Eq. 8), consequentially a smaller margin size should be chosen for larger N (Liu et al. 2020).

The different point distributions for $\partial\Omega_C$, $\partial\Omega_O$ and $\partial\Omega_I$ used in this study are shown in Fig. 4. The distances between the borders $\partial\Omega_C$ - $\partial\Omega_O$ and $\partial\Omega_O$ - $\partial\Omega_I$ are set to 300 km. Different distances between 50 km and 500 km were tested and the chosen 300 km have shown to be sufficient to avoid edge effects from the RBF modelling within the investigation area.

While the simulated observation data for the Kalman filter are given as gridded EWH time series, in the Kalman filter itself the computation is based on RBFs, leading to the output being a set of coefficients a_k for each time step. For the evaluation of EWH changes, the RBF coefficients are converted back to gridded EWH time series. This conversion between the different parameterisations, even without the Kalman filter computations, is not error-free, thus an uncertainty arises solely from the conversion itself. Since the shape of the RBF coefficients is determined by the expected gravity field signal content (300 km Gaussian filtered residual ESA ESM degree amplitudes), the introduction of noise in the simulated observations $\mathbf{l}$ leads to parts of the noisy signal not being included in the parameter space that can be mapped with the RBFs. This implies that a conversion error $\hat{\mathbf{e}}$ occurs during the conversion from gridded data to RBF coefficients a_k, which can be computed using the orthogonal projection operator as described by Koch (1999) according to

$$\hat{\mathbf{e}} = -(\mathbf{I} - \mathbf{A}\left(\mathbf{A}^T\mathbf{A}\right)^{-1}\mathbf{A}^T)\mathbf{l} = \hat{\mathbf{l}} - \mathbf{l} \tag{9}$$

where the matrix $\mathbf{A}$ contains the $\Phi_k(\mathbf{x}, \mathbf{x}_k)$ from Eq. 6 and $\mathbf{l}$ are the Gaussian-filtered, noisy gridded values from Eq. 4.

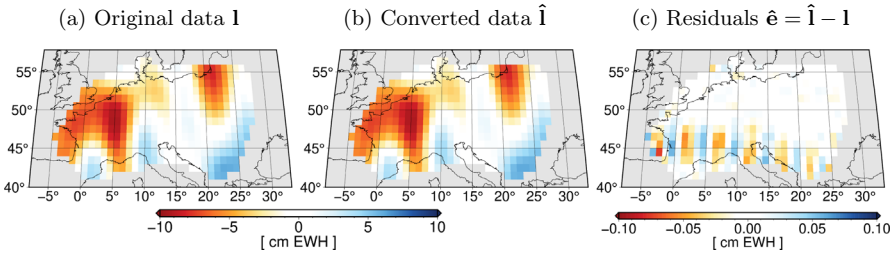

Fig. 5 RBF conversion (from gridded data $\mathbf{l}$ (left) to RBF and back to gridded data $\hat{\mathbf{l}}$ (centre)) and conversion error $\hat{\mathbf{e}} = -(\mathbf{I} - \mathbf{A}(\mathbf{A}^T\mathbf{A})^{-1}\mathbf{A}^T)\mathbf{l}$ (right) using 300 km Gaussian-filtered, noisy observation data for one exemplary month (2006-02)

Figure 5a shows the gridded data $\mathbf{l}$ (300 km Gaussian-filtered, with added noise) for one exemplary month, which are converted to the RBF representation (i.e. a set of coefficients a_k), and then converted back to gridded data $\hat{\mathbf{l}} = \mathbf{A}\left(\mathbf{A}^T\mathbf{A}\right)^{-1}\mathbf{A}^T\mathbf{l}$, as shown in Fig. 5b. The differences between the two sets of gridded data (Fig. 5a vs. Figure 5b) are hardly visible and become noticeable only when computing the residuals according to $\hat{\mathbf{e}} = \hat{\mathbf{l}} - \mathbf{l}$ and adjusting the colour scale in Fig. 5c by a factor of 100. When comparing the residuals in Fig. 5c to the error pattern of the GRACE input signal (see Fig. 2) it becomes clear that the stripes in the residuals are smaller in their east–west extent and are mainly influenced by the spatial distribution of the RBFs (see Fig. 4). The residuals $\hat{\mathbf{e}}$ range from -0.7 mm EWH to 0.6 mm EWH, with an area-weighted spatial RMS of all grid cells of 0.2 mm EWH for this exemplary month. Repeating this computation for all months and computing the mean RMS for all time steps results in a mean spatial RMS of 0.4 mm EWH, i.e. slightly larger than the exemplary month shown in Fig. 5, which can be considered the mean conversion error. The mean spatial RMS of the simulated observations on the other hand is 37.4 mm EWH, which means that the conversion error RMS is only about 1 % of the observation RMS.

4 Kalman filter framework

The Kalman filter, first introduced in 1960 by Rudolph Kalman (Kalman 1960), was developed to combine noisy observations in the framework of a recursive least-squares adjustment to compute an optimal estimate (Simon 2006). It consists of an observation model and a process model, which together form a linear dynamic system in which the current state vector $\hat{\mathbf{x}}_i$ is estimated for each epoch i by combining the (noisy) observations with the information from the process model and the state vector from the previous epoch $i-1$. The computational process of the Kalman filter itself follows the approach introduced by Kurtenbach et al. (2009), later refined (Kurtenbach et al. 2012) and also used by Kvas (2020) and is based on normal equations, see Appendix A.

The observation model contains the observations that are used in the Kalman filter. Via the functional matrix $\mathbf{A}_i$, the observations $\mathbf{l}_i$ are linked to the unknown parameters $\mathbf{x}_i$ which describe the gravity field at epoch i. Together with the corrections $\mathbf{v}_i$ the

following overdetermined system of linear equations results:

$$\mathbf{l}_i = \mathbf{A}_i \mathbf{x}_i + \mathbf{v}_i \quad \text{with} \quad \mathbf{v}_i \sim \mathcal{N}(\mathbf{0}, \mathbf{R}_i). \tag{10}$$

It is assumed that the expected values of the corrections $\mathbf{v}_i$ are $\mathbf{0}$ and the corresponding covariance matrix of the corrections is given by $\mathbf{R}_i$. In the Kalman filter set up here, the calculated time series from Eq. 4 are used for the observations $\mathbf{l}_i$, the functional matrix $\mathbf{A}_i$ contains the $\Phi_k(\mathbf{x}, \mathbf{x}_k)$ from Eq. 6 and the observation covariance matrix $\mathbf{R}_i$ is the Gaussian-filtered GRACE covariance matrix of the grid values as shown in Fig. 1.

The process model used in this study is based on the least-squares prediction (Moritz 1989), whereby the naming conventions follow the work of Kurtenbach (2011), and represents the second part of the Kalman filter. It approximates the temporal behaviour of the Earth's gravity field using stochastic information from geophysical models based on the assumption that the gravity field does not change arbitrarily from one epoch to the next, but is predictable during a certain period of integration. The process model thus describes the expected variability of the state vector $\hat{\mathbf{x}}_i^-$ and predicts the changes of the gravity field from one epoch $\mathbf{x}_{i-1}$ to the subsequent epoch $\mathbf{x}_i$ using a first order discrete Markov process according to

$$\mathbf{x}_i = \mathbf{B}\mathbf{x}_{i-1} + \mathbf{w} \quad \text{with} \quad \mathbf{w} \sim \mathcal{N}(\mathbf{0}, \mathbf{Q}), \tag{11}$$

with the time-constant state transition matrix $\mathbf{B}$ and associated stochastic process noise $\mathbf{w}$ of the modelled state vector, which describes the inaccuracies of the model with the expected values $\mathbf{0}$ and covariance matrix $\mathbf{Q}$. The state transition matrix $\mathbf{B}$ and covariance matrix of the process noise $\mathbf{Q}$ are computed using the full correlation structure between two subsequent time steps $i-1$ and i:

$$\mathcal{C}\left\{\begin{pmatrix}\mathbf{x}_i \\ \mathbf{x}_{i-1}\end{pmatrix}\right\} = \begin{pmatrix}\boldsymbol{\Sigma} & \boldsymbol{\Sigma}_\Delta \\ \boldsymbol{\Sigma}_\Delta^T & \boldsymbol{\Sigma}\end{pmatrix} \tag{12}$$

where $\boldsymbol{\Sigma}$ is the auto covariance matrix

$$\boldsymbol{\Sigma} := \mathcal{C}\{\mathbf{x}_i, \mathbf{x}_i\} \tag{13}$$

which describes the spatial variability of the expected gravity field, while the cross covariance matrix $\boldsymbol{\Sigma}_\Delta$ describes the temporal variability from one time step to the next:

$$\boldsymbol{\Sigma}_\Delta := \mathcal{C}\{\mathbf{x}_i, \mathbf{x}_{i-1}\}. \tag{14}$$

The state transition matrix $\mathbf{B}$ can be computed according to

$$\mathbf{B} = \boldsymbol{\Sigma}_\Delta \boldsymbol{\Sigma}^{-1} \tag{15}$$

which is based on the requirement that the error covariance matrix associated with the error vector of the estimator $\mathbf{B}$ in Eq. 11 becomes minimal. The covariance matrix $\mathbf{Q}$ of the process noise $\mathbf{w}$ is then given by

$$\mathbf{Q} = \boldsymbol{\Sigma} - \boldsymbol{\Sigma}_{\Delta}\boldsymbol{\Sigma}^{-1}\boldsymbol{\Sigma}_{\Delta}^{T}. \tag{16}$$

Since the true states of the Earth's gravity field are not known, $\boldsymbol{\Sigma}$ and $\boldsymbol{\Sigma}_{\Delta}$ can only be approximated empirically from geophysical models. For this, the residual ESA ESM time series $\tilde{\mathbf{v}}_i$ as described in Eq. 1 is used. The time series is again filtered with a 300 km Gaussian filter and converted to RBF scaling coefficients $\mathbf{a}_i$ (see Eq. 5, each vector $\mathbf{a}_i$ contains the K scaling coefficients a_k for time step i) before computing the approximated covariance matrices $\bar{\boldsymbol{\Sigma}}$ and $\bar{\boldsymbol{\Sigma}}_{\Delta}$. The time series thus consist of I state vectors $\mathbf{a}_i$ containing the scaling coefficients:

$$\mathbf{x}_i \approx \mathbf{m}_i = \mathbf{a}_i^T. \tag{17}$$

From these state vectors at time points i, the empirical auto covariance matrix

$$\boldsymbol{\Sigma} \approx \bar{\boldsymbol{\Sigma}} = \frac{1}{I}\sum_{i=1}^{I}\mathbf{m}_i\mathbf{m}_i^T \tag{18}$$

and empirical cross covariance matrix

$$\boldsymbol{\Sigma}_{\Delta} \approx \bar{\boldsymbol{\Sigma}}_{\Delta} = \frac{1}{I-1}\sum_{i=2}^{I}\mathbf{m}_i\mathbf{m}_{i-1}^T \tag{19}$$

can be computed, which then can represent the temporal behaviour of the Earth's gravity field given in Eq. 11. At this point, it should be emphasised that this is a purely stochastic process model, as discussed in Kurtenbach (2011). This means that only stochastic information is derived from the geophysical model rather than using the model output directly.

5 Simulation results

To assess the performance of the Kalman filter results, the simulation output is compared to a reference, which in this case are the 300 km Gaussian-filtered time series from the ESA ESM. As described in Sect. 2, in order to simulate the GRACE observations, correlated noise is added to the filtered time series, which is to be minimised using the Kalman filter. Therefore, the goal is that the Kalman-filtered time series is as close as possible to the 300 km Gaussian-filtered reference time series.

The evaluation of the results is done both in the time and spatial domain. The time series are assessed using the evaluation metrics correlation coefficient to determine the linear relationship between the data, and root mean squared deviation (RMSD) to show how well the different data sets fit together in terms of absolute differences.

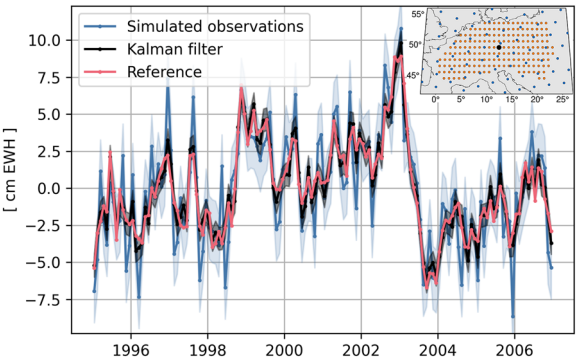

Fig. 6 Exemplary grid cell time series at 12.5° E, 49.5° N, see black dot in the small map. Reference data (red), noisy simulated observation data (blue, including error band in light blue) and Kalman-filtered time series (black, including error band in dark grey) (colour figure online)

Figure 6 shows the time series for the simulated observation (blue), Kalman-filtered (black) and reference (red) data for an exemplary grid cell of size $1° \times 1°$ in the centre of the investigation area (12.5° E, 49.5° N). While the simulated observations show distinct deviations from the reference time series due to the added noise with a correlation coefficient of 0.84 for this grid cell, the Kalman-filtered time series fits much better to the reference. This shows the ability of the Kalman filter to minimise most of the added noise, which is also indicated by the much higher correlation coefficient of 0.98. The good agreement between the time series is also reflected in the RMSD with respect to the reference time series, which is 2.02 cm EWH for the observations and much lower and thus better for the Kalman filter result with 0.62 cm EWH. As also visually apparent, the temporal RMS of the reference (3.11 cm EWH) and Kalman-filtered time series (3.10 cm EWH) are similar, while it is slightly larger for the simulated observations (3.72 cm EWH). If instead of the grid cell in the centre of the investigation area a grid cell at the edge is selected, the results of the agreement are very similar, so that the grid cell shown is representative for the area.

In addition to the time series also the error bars are plotted for the observations (light blue band) and for the Kalman filter result (dark grey band). The former are derived by error propagation from the covariance matrix $\mathbf{R}_i$ of the observations, see Eq. 10, and the latter from the a posteriori covariance matrix $\mathbf{P}_i^+$ of the Kalman filter update, see Eq. A8 in the appendix. The standard deviation of the observation amounts to around 2.13 cm EWH, while the post-fit standard deviation is considerably smaller with around 0.77 cm EWH. Furthermore, almost all points of the time series of the reference signal (red curve) lie within the estimated error bars of the Kalman filter update.

While the time series shown in Fig. 6 provide a comparison of the data in the temporal domain for one particular grid cell, Fig. 7 shows the gridded data in the spatial domain for an exemplary month (2006–02) for the simulated observations (Fig. 7a), the Kalman filter result (Fig. 7b), and the difference between the Kalman filter result and the reference data (Fig. 7c), all of them evaluated in the investigation area $\partial\Omega_I$. From Fig. 7 it can be seen that the Kalman filter result is very similar to the reference data, as shown by the differences between the two data sets, which are an order of magnitude smaller than the signal itself. The GRACE-like noise stripes as

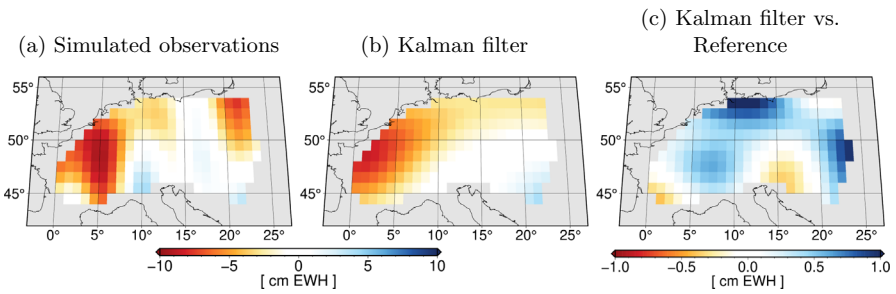

Fig. 7 Noisy observation data (left), Kalman-filtered result (centre) and difference Kalman-filtered minus reference data (right) in evaluation area $\partial\Omega_I$ for one exemplary time step (2006-02)

in the simulated observations are no longer present in the result of the Kalman filter, indicating its ability to effectively minimise the noise.

However, the Kalman filter result grid contains slightly lower absolute values than the reference, as can be seen from Fig. 7c. The differences between the individual grid cell values (Kalman filter result minus reference) range from −0.40 cm to 1.10 cm EWH with a spatial RMS of the differences of 0.44 cm EWH. The lower absolute values can also be seen when comparing the three monthly grids (simulated observations vs. Kalman filter result vs. reference) in terms of the spatial RMS, which shows that the Kalman filter result with an RMS of 3.48 cm EWH is lower compared to the simulated observations with an RMS of 4.07 cm EWH, and also slightly lower compared to the reference data with 3.72 cm EWH for this exemplary month.

Figure 7 shows only one snapshot for a specific month (2006-02). To take all time steps into account, the mean RMS (i.e. the temporally averaged spatial RMS) can be calculated for each of the three data sets. The simulated observations yield a mean RMS of 3.83 cm EWH, while the Kalman filter and the reference data both have a mean RMS of 3.12 cm EWH. Despite having the same mean RMS, the individual monthly grids of the Kalman filter result and the reference can still be different from each other. This can be concluded from the mean RMS of the difference between the Kalman filter and the reference being 0.59 cm EWH. The larger RMS value of the simulated observations is attributed to the introduction of correlated noise, which is effectively minimised using the Kalman filter, so both the Kalman filter and reference data sets show the same variability.

For a further evaluation of the Kalman filter results for all time steps in the whole investigation area $\partial\Omega_I$, the correlation coefficient and RMSD in the temporal domain are computed for all grid cells, i.e. the analysis of the exemplary grid cell time series (Fig. 6) is carried out for all grid cells. Figure 8 displays the two evaluation metrics correlation coefficient (top row) and RMSD (bottom row) in the investigation area $\partial\Omega_I$.

The area-weighted mean temporal correlation with respect to the reference data is 0.83 for the simulated observations and 0.98 for the Kalman filter result and thus much higher as can clearly be seen in Figs. 8a and 8b. The increase of the correlation coefficient for the individual grid cells ranges from 0.08 to 0.27. The area-weighted mean RMSD with respect to the the reference is 2.16 cm EWH for the simulated obser-

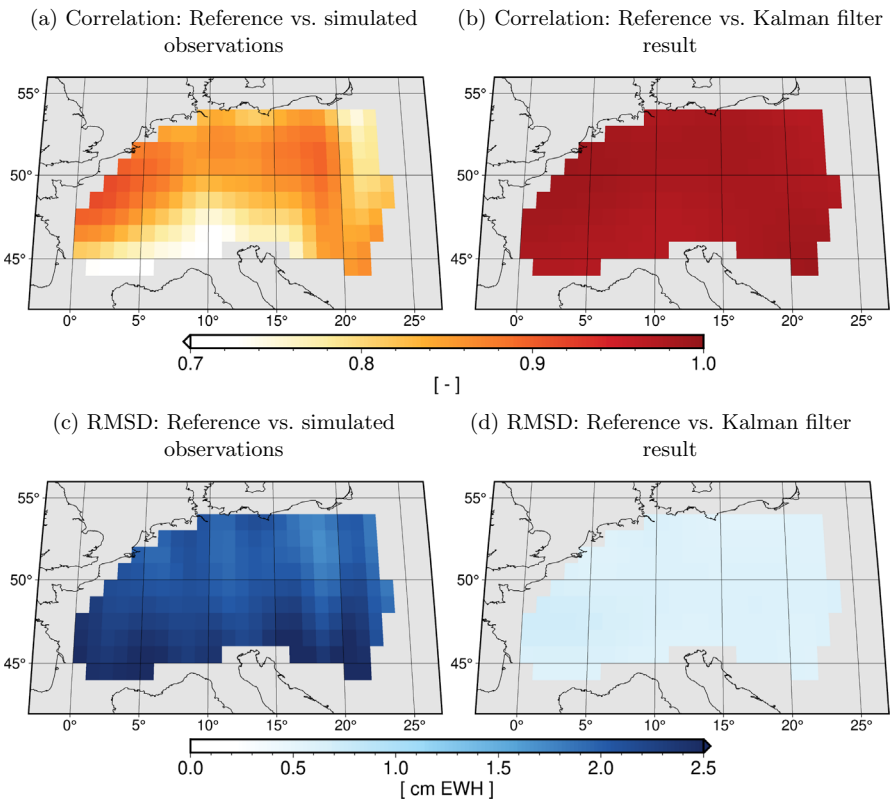

Fig. 8 Computed correlation coefficients (top) and RMSD values (bottom) between the reference time series and the simulated observation time series shown on the left (Figs. 8a and 8c) and between the reference time series and the Kalman-filtered time series on the right (Figs. 8b and 8d) for all grid cells in the evaluation area $\partial\Omega_I$

vations (Fig. 8c) and decreases to 0.62 cm EWH for the Kalman filter result (Fig. 8d), where the individual RMSD grid cell values decrease by 1.12 cm to 2.10 cm EWH. The improvement in correlation shows that there is a strong linear relation between the grid cell time series of the Kalman filter and the reference signal. The decrease in RMSD implicates that also the absolute differences between the Kalman filter and reference have strongly improved compared to the noisy observations.

As shown in Fig. 6 and calculated for the exemplary grid cell, the observation accuracies from $\mathbf{R}_i$ and the a posteriori accuracies of the Kalman filter updates from $\mathbf{P}_i^+$ can be variance propagated for all grid cells. The comparison shows that the standard deviations of the Kalman filter for the individual grid cells lie between 0.69 and 0.81 cm EWH and is thus considerably smaller than the standard deviations of the observations, which lie between 1.92 and 2.55 cm EWH.

If the calculations are carried out with the RBF shape coefficients φ_n (see Eq. 6) that use the degree amplitudes σ_n from Kaula's rule instead of the empirical σ_n from the ESA ESM data, the Kalman filter gives similar results with only minor changes of

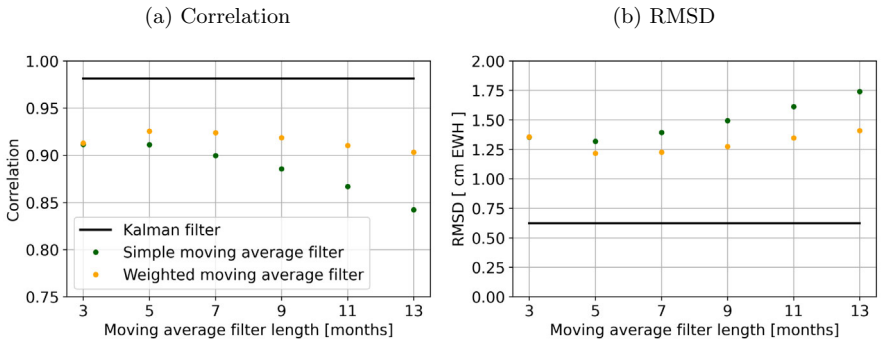

Fig. 9 Area-weighted mean correlation (left) and RMSD (right) between all time steps of reference and Kalman filter (black), simple moving average filter (green) and weighted moving average filter (orange) for filter lengths 3 – 13 months (colour figure online)

the evaluation metrics with respect to the reference. The mean correlation coefficient deviates by 0.07 % and the RMSD by 1.18 % when using the φ_n from Kaula's rule instead of those defined by Eq. 6. This emphasises the invariance of the Kalman filter result in this simulation framework to the specific choice of degree amplitudes from which the RBF shape coefficients are derived.

To investigate whether a simple boxcar (simple moving average, SMA) or weighted moving average (WMA) filter could achieve similarly good results as the Kalman filter approach, we tested different filter lengths of SMA and WMA filters. The comparison with the reference is shown in Fig. 9, again in terms of the (area-weighted) mean correlation coefficient (Fig. 9a) and the mean RMSD in the investigation area (Fig. 9b). The different filter lengths of the moving average filters ranging from 3 to 13 months are shown on the x-axis and the respective evaluation metrics are displayed on the y-axis. The agreement of the Kalman filter with the reference is shown by the constant black line, since no different filter lengths are applied.

The SMA filter is computed using the same filter weights for all months included in the computation of the average, i.e. weights $\frac{1}{3}, \frac{1}{3}, \frac{1}{3}$ for 3 months and similarly for the other number of months. The resulting agreement with the reference time series is shown in green. The WMA filter gives a higher weight to the current month and lower weights to the preceding and subsequent months, i.e. weights $\frac{1}{4}, \frac{2}{4}, \frac{1}{4}$ for 3 months, $\frac{1}{9}, \frac{2}{9}, \frac{3}{9}, \frac{2}{9}, \frac{1}{9}$ for 5 months and so forth, with the results displayed in orange.

Figure 9a shows that the correlation for both the SMA and WMA filter is lower than that of the Kalman filter. However, the moving average filters also exhibit large correlations with the reference time series. The WMA filter outperforms the SMA filter for all choices of filter lengths showing the best performance at 5 months with a correlation of 0.93 (SMA: 0.91), compared to a correlation of 0.98 for the Kalman filter. Comparing the RMSD values makes the added value of the Kalman filter setup even more evident. The agreement with respect to the reference is 0.62 cm EWH for the Kalman filter, and considerably lower for both moving average filters. This is reflected by the larger RMSD values, ranging from 1.32 cm to 1.74 cm EWH for the SMA filter and 1.22 cm to 1.41 cm EWH for the WMA filter. Both filters again demonstrate

their best performance at a filter length of 5 months. Filtering always represents a compromise between filtering out noise and retaining as much signal as possible, with this ratio being optimal for a filter length of 5 months in the present example and gradually decreasing with increasing filter length. However, no specific geophysical meaning is attributed to this number.

The results hence indicate that the Kalman filter consistently outperforms both the simple and weighted moving average filters, indicating the strong added value of the additional information contained in the process model and uncertainties that are used in the Kalman filter.

6 Summary and conclusions

In this study, a parameter estimation framework was developed that allows the estimation of regional (water) mass variations from geodetic observations based on a tailored regional parameterisation introducing for the first time radial basis functions into a Kalman filter estimation procedure for gravity field parameters. To demonstrate the feasibility and robustness of the approach, a closed-loop simulation framework has been set up, which employs time-variable simulated GRACE data in a test region located in central Europe. The simulated observation data used in our study are derived from the ESA Earth System Model, filtered with a 300 km Gaussian filter and then corrupted by realistic correlated noise derived from a real GRACE covariance matrix. The process model implemented in the Kalman filter introduces the predicted behaviour of the residual gravity field using stochastic information from the ESA ESM. To compute water mass changes in the investigation area, a regional modelling approach using space-localising radial basis functions is implemented in the Kalman filter, which offers the advantage of a parameterisation with high spatial resolution using only a small number of parameters. It also allows to incorporate observables which are only locally or regionally available. The shape of the RBF coefficients φ_n reflects the general spectral characteristics of the gravity field and is also derived from ESA ESM data in this study. However, using Kaula's rule for the computation of the coefficients φ_n yields comparable results.

A comparison to the reference (simulated data without added noise) shows a very high agreement of the Kalman-filtered time series with a correlation coefficient of 0.98 and RMSD of 0.62 cm EWH, demonstrating the ability of the Kalman filter to minimise the added noise. This also manifests when comparing the temporally averaged spatial RMS, which is 3.83 cm EWH for the simulated observations and 3.12 cm EWH both for the Kalman filter and reference data. The comparison to less sophisticated filters such as a simple and weighted moving average filter shows that the Kalman filter result outperforms both filters, proving the added value of the incorporation of the process model and of the uncertainties in the Kalman filter framework. Compared to a global spherical harmonic representation, the number of unknown parameters to be estimated in each time step is only about 1 % of the coefficients needed for a spherical harmonic expansion of equivalent spatial resolution (i.e. the fraction of the Earth's surface covered by our investigation area). In our current simulation experiment the estimation of 9.409 spherical harmonic parameters (corresponding to a maximum expansion degree

of 96) instead of 106 RBF coefficients would of course be possible. However, the targeted future increase of the spatial resolution when including additional observation types to achieve, e.g. a 50 km – 100 km resolution or below, would easily lead to the demand of estimating several hundred of thousands of global coefficients per time step, which demonstrates the computational advantage of regional modelling. As a proof of concept, we repeated the analysis using the same regional observations, but exchanging the parameterisation to spherical harmonics. The results are almost identical, which give confidence that the regional modelling provides reasonable results. Please note that throughout our simulation post-processed (filtered) global models were used as input data and it can thus not be expected that the regional processing is able to extract any additional information from these data compared to a global modelling. Furthermore, it was not the goal of this study to show that regional modelling provides superior results over a global representation.

By implementing the Kalman filter in a closed-loop simulation environment, a stable framework with a functional process model was created that can be used for the calculation of time-variable, regional gravity fields with high spatio-temporal resolution. The implementation of the Kalman filter based on normal equations enables the flexible and successive integration of other observation types with varying temporal and spatial resolution such as GNSS and terrestrial gravimetry. The closed-loop simulation environment provides a solid basis for future applications of real data. Furthermore, it is possible to extend the Kalman filter with the direct implementation of GRACE and GRACE-FO Level 1B data. So far, we have used gridded, post-processed (filtered) global spherical harmonic time series as input for our Kalman filter. However, this global post-processing prevents the optimal extraction of regional signal content in a specific area. In earlier studies (e.g. Eicker 2008; Eicker et al. 2009), it was shown that a direct tailored regional processing, which directly estimates the scaling coefficients of the RBFs from the inter-satellite ranging observations, allows to extract additional high-resolution information from the observations.

Appendix A Kalman filter

The first step of the Kalman filter procedure is the prediction, in which the state vector of the current epoch $\hat{\mathbf{x}}_i^-$ is predicted using the previous state vector $\hat{\mathbf{x}}_{i-1}^+$ and the state transition matrix $\mathbf{B}$:

$$\hat{\mathbf{x}}_i^- = \mathbf{B}\hat{\mathbf{x}}_{i-1}^+. \tag{A1}$$

The covariance of the prediction $\mathbf{P}_i^-$ is calculated by variance propagation using the accuracy of the previous step $\mathbf{P}_{i-1}^+$, with the addition of the process noise $\mathbf{Q}$, since the process dynamic cannot be assumed to be error-free:

$$\mathbf{P}_i^- = \mathbf{B}\mathbf{P}_{i-1}^+\mathbf{B}^T + \mathbf{Q}. \tag{A2}$$

The second computational step of the Kalman filter procedure is the update, for which different algorithms can be used, all of which give the same result. One approach is

based on the computation of the Kalman gain matrix $\mathbf{K}_i$, which is used to weight the prediction $\hat{\mathbf{x}}_i^-$ and the observations $\mathbf{l}_i$ based on their covariance matrices:

$$\mathbf{K}_i = \mathbf{P}_i^- \mathbf{A}_i^T \left(\mathbf{R}_i + \mathbf{A}_i \mathbf{P}_i^- \mathbf{A}_i^T \right)^{-1}. \tag{A3}$$

The difference $\mathbf{d}_i = \mathbf{l}_i - \mathbf{A}_i \hat{\mathbf{x}}_i^-$ between the prediction $\hat{\mathbf{x}}_i^-$ and the observations $\mathbf{l}_i$, also referred to as innovation, is scaled by $\mathbf{K}_i$ and added to the prediction $\hat{\mathbf{x}}_i^-$ to compute the update $\hat{\mathbf{x}}_i^+$ and its covariance matrix $\mathbf{P}_i^+$:

$$\hat{\mathbf{x}}_i^+ = \hat{\mathbf{x}}_i^- + \mathbf{K}_i \left(\mathbf{l}_i - \mathbf{A}_i \hat{\mathbf{x}}_i^- \right) \quad \text{and} \quad \mathbf{P}_i^+ = (\mathbf{I} - \mathbf{K}_i \mathbf{A}_i) \, \mathbf{P}_i^-. \tag{A4}$$

The second approach, which is used in this study, is based on normal equations in which a functional relationship, given in Eq. 10, is established between the observations $\mathbf{l}_i$ and the parameters $\mathbf{x}_i$ describing the gravity field. By inserting and transforming the system of normal equations

$$\mathbf{N}_i \mathbf{x}_i = \mathbf{n}_i \tag{A5}$$

with

$$\mathbf{N}_i = \mathbf{A}_i^T \mathbf{R}_i^{-1} \mathbf{A}_i \quad \text{and} \quad \mathbf{n}_i = \mathbf{A}_i^T \mathbf{R}_i^{-1} \mathbf{l}_i \tag{A6}$$

into the classical Kalman filter approach using the Kalman gain matrix then results in the formula

$$\hat{\mathbf{x}}_i^+ = \hat{\mathbf{x}}_i^- + \mathbf{P}_i^+ \left(\mathbf{n}_i - \mathbf{N}_i \hat{\mathbf{x}}_i^- \right) \tag{A7}$$

for computing the new predicted system state $\hat{\mathbf{x}}_i^+$. The corresponding covariance matrix of the update $\mathbf{P}_i^+$ is then calculated by

$$\mathbf{P}_i^+ = \left(\left(\mathbf{P}_i^- \right)^{-1} + \mathbf{N}_i \right)^{-1}. \tag{A8}$$

The detailed reformulation for this can be found e.g. in Kurtenbach (2011).

Acknowledgements This work was funded by the Deutsche Forschungsgemeinschaft (DFG, German Research Foundation) - Project ID 434617780 - SFB 1464 (Relativistic and quantum-based geodesy (TerraQ), subproject C05) and funded by the Deutsche Forschungsgemeinschaft (DFG, German Research Foundation) under Germany's Excellence Strategy - EXC-2123 QuantumFrontiers - 390837967.

Funding Open Access funding enabled and organized by Projekt DEAL.

Declarations

Conflict of interest The authors have no conflict of interest to declare that are relevant to the content of this article.

References

Argus, D.F., Fu, Y., Landerer, F.W.: Seasonal variation in total water storage in California inferred from GPS observations of vertical land motion. Geophys. Res. Lett. **41**(6), 1971–1980 (2014). https://doi.org/10.1002/2014GL059570

Bentel, K., Schmidt, M., Gerlach, C.: Different radial basis functions and their applicability for regional gravity field representation on the sphere. Int. J. Geomath. **4**(1), 67–96 (2013). https://doi.org/10.1007/s13137-012-0046-1

Dobslaw, H., Bergmann-Wolf, I., Dill, R., Forootan, E., Klemann, V., Kusche, J., Sasgen, I.: The updated ESA earth system model for future gravity mission simulation studies. J. Geod. **89**(5), 505–513 (2015). https://doi.org/10.1007/s00190-014-0787-8

Eicker, A., Mayer-Gürr, T., Ilk, K.-H.: Improved resolution of a grace gravity field model by regional refinements. In: Observing Our Changing Earth, Springer: London. pp. 99–104 (2009)

Eicker, A.: Gravity field refinement by radial basis functions from in-situ satellite data. PhD thesis, University of Bonn (2008). https://hdl.handle.net/20.500.11811/3245

Eicker, A., Schall, J., Kusche, J.: Regional gravity modelling from spaceborne data: Case studies with GOCE. Geophys. J. Int. **196**(3), 1431–1440 (2014). https://doi.org/10.1093/gji/ggt485

Ellmer, M.: Contributions to GRACE Gravity Field Recovery. PhD thesis, Graz University of Technology (2018). https://doi.org/10.3217/978-3-85125-646-8

Farrell, W.E.: Deformation of the Earth by surface loads. Rev. Geophys. **10**(3), 761–797 (1972). https://doi.org/10.1029/RG010i003p00761

Flechtner, F., Neumayer, K.-H., Dahle, C., Dobslaw, H., Fagiolini, E., Raimondo, J.-C., Güntner, A.: In: Cazenave, A., Champollion, N., Benveniste, J., Chen, J. (eds.) What Can be Expected from the GRACE-FO Laser Ranging Interferometer for Earth Science Applications?, pp. 263–280. Springer, Cham (2016). https://doi.org/10.1007/978-3-319-32449-4_11

Freeden, W., Törnig, W.: On spherical spline interpolation and approximation. Math. Methods Appl. Sci. **3**(1), 551–575 (1981). https://doi.org/10.1002/mma.1670030139

Güntner, A., Reich, M., Mikolaj, M., Creutzfeldt, B., Schroeder, S., Wziontek, H.: Landscape-scale water balance monitoring with an iGrav superconducting gravimeter in a field enclosure. Hydrol. Earth Syst. Sci. **21**(6), 3167–3182 (2017). https://doi.org/10.5194/hess-21-3167-2017

Han, S., Simons, F.J.: Spatiospectral localization of global geopotential fields from the gravity recovery and climate experiment (GRACE) reveals the coseismic gravity change owing to the 2004 Sumatra–Andaman earthquake. J. Geophys. Res. Solid Earth **113**, B1 (2008). https://doi.org/10.1029/2007JB004927

Harig, C., Simons, F.J.: Mapping Greenland's mass loss in space and time. Proc. Natl. Acad. Sci. U.S.A. **109**(49), 19934–19937 (2012). https://doi.org/10.1073/pnas.1206785109

Heiskanen, W.A., Moritz, H.: Physical Geodesy. W. H. Freeman, San Francisco (1967). https://doi.org/10.1007/BF02525647

Kalman, R.E.: A new approach to linear filtering and prediction problems. J. Basic. Eng. **82**(1), 35–45 (1960). https://doi.org/10.1115/1.3662552

Kaula, W.M.: Theory of Satellite Geodesy. Blaisdell Publishing Company, Waltham, MA (1966)

Koch, K.-R.: Parameter Estimation and Hypothesis Testing in Linear Models. Springer Berlin Heidelberg, Berlin, Heidelberg (1999).https://doi.org/10.1007/978-3-662-03976-2

Kurtenbach, E., Mayer-Gürr, T., Eicker, A.: Deriving daily snapshots of the Earth's gravity field from GRACE L1B data using Kalman filtering. Geophys. Res. Lett. **36**(17) (2009) https://doi.org/10.1029/2009GL039564

Kurtenbach, E.: Entwicklung eines Kalman-Filters zur Bestimmung kurzzeitiger Variationen des Erdschwerefeldes aus Daten der Satellitenmission GRACE. PhD thesis, University of Bonn (2011). https://hdl.handle.net/20.500.11811/4734

Kurtenbach, E., Eicker, A., Mayer-Gürr, T., Holschneider, M., Hayn, M., Fuhrmann, M., Kusche, J.: Improved daily GRACE gravity field solutions using a Kalman smoother. J. Geodyn. **59–60**, 39–48 (2012). https://doi.org/10.1016/j.jog.2012.02.006

Kvas, A.: Estimation of High-Frequency Mass Variations from Satellite Data in near Real-Time Implementation of a Technology Demonstrator for near Real-Time GRACE/GRACE-FO Gravity Field Solutions. PhD thesis, Graz University of Technology (2020). https://doi.org/10.3217/978-3-85125-771-7

Kvas, A., Mayer-Gürr, T.: Grace gravity field recovery with background model uncertainties. J. Geod. **93**(12), 2543–2552 (2019)

Kvas, A., Behzadpour, S., Ellmer, M., Klinger, B., Strasser, S., Zehentner, N., Mayer-Gürr, T.: ITSG–Grace2018: overview and evaluation of a new GRACE–only gravity field time series. J. Geophys. Res. Solid Earth **124**(8), 9332–9344 (2019). https://doi.org/10.1029/2019JB017415

Landerer, F.W., Flechtner, F.M., Save, H., Webb, F.H., Bandikova, T., Bertiger, W.I., Bettadpur, S.V., Byun, S.H., Dahle, C., Dobslaw, H., Fahnestock, E., Harvey, N., Kang, Z., Kruizinga, G.L.H., Loomis, B.D., McCullough, C., Murböck, M., Nagel, P., Paik, M., Pie, N., Poole, S., Strekalov, D., Tamisiea, M.E., Wang, F., Watkins, M.M., Wen, H., Wiese, D.N., Yuan, D.: Extending the global mass change data record: GRACE follow-on instrument and science data performance. Geophys. Res. Lett. **47**(12), 306 (2020). https://doi.org/10.1029/2020GL088306

Lisdat, C., Grosche, G., Quintin, N., Shi, C., Raupach, S.M.F., Grebing, C., Nicolodi, D., Stefani, F., Al-Masoudi, A., Dörscher, S., Häfner, S., Robyr, J.-L., Chiodo, N., Bilicki, S., Bookjans, E., Koczwara, A., Koke, S., Kuhl, A., Wiotte, F., Meynadier, F., Camisard, E., Abgrall, M., Lours, M., Legero, T., Schnatz, H., Sterr, U., Denker, H., Chardonnet, C., Le Coq, Y., Santarelli, G., Amy-Klein, A., Le Targat, R., Lodewyck, J., Lopez, O., Pottie, P.-E.: A clock network for geodesy and fundamental science. Nat. Commun. **7**, 12443 (2016). https://doi.org/10.1038/ncomms12443

Liu, Q., Schmidt, M., Sánchez, L., Willberg, M.: Regional gravity field refinement for (quasi-) geoid determination based on spherical radial basis functions in Colorado. J. Geod. **94**(10), 431 (2020). https://doi.org/10.1007/s00190-020-01431-2

Loomis, B.D., Luthcke, S.B., Sabaka, T.J.: Regularization and error characterization of GRACE mascons. J. Geod. **93**(9), 1381–1398 (2019). https://doi.org/10.1007/s00190-019-01252-y

Mayer-Gürr, T., Behzadpur, S., Ellmer, M., Kvas, A., Klinger, B., Strasser, S., Zehentner, N.: ITSG-Grace2018 - Monthly, Daily and Static Gravity Field Solutions from GRACE. GFZ Data Services (2018). https://doi.org/10.5880/ICGEM.2018.003

Mayer-Gürr, T.: Gravitationsfeldbestimmung aus der Analyse kurzer Bahnbögen am Beispiel der Satellitenmissionen CHAMP und GRACE. PhD thesis, University of Bonn (2006). https://hdl.handle.net/20.500.11811/1391

Mayer-Gürr, T., Behzadpour, S., Eicker, A., Ellmer, M., Koch, B., Krauss, S., Pock, C., Rieser, D., Strasser, S., Süsser-Rechberger, B., Zehentner, N., Kvas, A.: GROOPS: a software toolkit for gravity field recovery and GNSS processing. Comput. Geosci. **155**, 104864 (2021). https://doi.org/10.1016/j.cageo.2021.104864

Moritz, H.: Advanced Physical Geodesy, 2. ed., reprint. from the 1. ed edn. Wichmann, Karlsruhe (1989)

Müller, J., Dirkx, D., Kopeikin, S.M., Lion, G., Panet, I., Petit, G., Visser, P.N.A.M.: High performance clocks and gravity field determination. Space Sci. Rev. **214**(1), 5 (2018). https://doi.org/10.1007/s11214-017-0431-z

Ramillien, G., Seoane, L., Schumacher, M., Forootan, E., Frappart, F., Darrozes, J.: Recovery of rapid water mass changes (RWMC) by Kalman filtering of GRACE observations. Remote Sens. **12**(8), 1299 (2020). https://doi.org/10.3390/rs12081299

Ramillien, G., Seoane, L., Darrozes, J.: An Innovative slepian approach to invert GRACE KBRR for localized hydrological information at the sub-basin scale. Remote Sens. **13**(9), 1824 (2021). https://doi.org/10.3390/rs13091824

Ran, J., Ditmar, P., Klees, R.: Optimal mascon geometry in estimating mass anomalies within Greenland from GRACE. Geophys. J. Int. **214**(3), 2133–2150 (2018). https://doi.org/10.1093/gji/ggy242

Rowlands, D.D., Luthcke, S.B., Klosko, S.M., Lemoine, F.G.R., Chinn, D.S., McCarthy, J.J., Cox, C.M., Anderson, O.B.: Resolving mass flux at high spatial and temporal resolution using GRACE intersatellite measurements. Geophys. Res. Lett. **32**(4), 904 (2005). https://doi.org/10.1029/2004GL021908

Save, H., Bettadpur, S., Tapley, B.D.: High-resolution CSR GRACE RL05 mascons. J. Geophys. Res. Solid Earth **121**(10), 7547–7569 (2016). https://doi.org/10.1002/2016JB013007

Schmidt, M., Han, S., Kusche, J., Sanchez, L., Shum, C.K.: Regional high-resolution spatiotemporal gravity modeling from GRACE data using spherical wavelets. Geophys. Res. Lett. **33**(8), 509 (2006). https://doi.org/10.1029/2005GL025509

Schrama, E.J.O., Wouters, B., Rietbroek, R.: A mascon approach to assess ice sheet and glacier mass balances and their uncertainties from GRACE data. J. Geophys. Res. Solid Earth **119**(7), 6048–6066 (2014). https://doi.org/10.1002/2013JB010923

Simon, D.: Optimal State Estimation: Kalman, H ∞, and Nonlinear Approaches. Wiley-Interscience, Hoboken, NJ (2006). https://doi.org/10.1002/0470045345

Swenson, S., Wahr, J.: Post-processing removal of correlated errors in GRACE data. Geophys. Res. Lett. **33**(8), 285 (2006). https://doi.org/10.1029/2005GL025285

Tapley, B.D., Bettadpur, S., Watkins, M., Reigber, C.: The gravity recovery and climate experiment: mission overview and early results. Geophys. Res. Lett. **31**(9), 20 (2004). https://doi.org/10.1029/2004GL019920

Tapley, B.D., Watkins, M.M., Flechtner, F., Reigber, C., Bettadpur, S., Rodell, M., Sasgen, I., Famiglietti, J.S., Landerer, F.W., Chambers, D.P., Reager, J.T., Gardner, A.S., Save, H., Ivins, E.R., Swenson, S.C., Boening, C., Dahle, C., Wiese, D.N., Dobslaw, H., Tamisiea, M.E., Velicogna, I.: Contributions of GRACE to understanding climate change. Nat. Clim. Change **9**, 358–369 (2019). https://doi.org/10.1038/s41558-019-0456-2

Vestine, E.H., Sibley, W.L., Kern, J.W., Carlstedt, J.L.: Integral and spherical-harmonic analyses of the geomagnetic field for 1955.0, PART 2. J. Geomagn. Geoelectr. **15**(2), 73–89 (1963). https://doi.org/10.5636/jgg.15.73

von Hippel, M., Harig, C.: Long-term and inter-annual mass changes in the Iceland ice cap determined from GRACE gravity using slepian functions. Front. Earth Sci. **7**, 171 (2019). https://doi.org/10.3389/feart.2019.00171

Wahr, J., Molenaar, M., Bryan, F.: Time variability of the Earth's gravity field: Hydrological and oceanic effects and their possible detection using GRACE. J. Geophys. Res. Solid Earth **103**(B12), 30205–30229 (1998). https://doi.org/10.1029/98JB02844

Watkins, M.M., Wiese, D.N., Yuan, D., Boening, C., Landerer, F.W.: Improved methods for observing Earth's time variable mass distribution with GRACE using spherical cap mascons. J. Geophys. Res. Solid Earth **120**(4), 2648–2671 (2015). https://doi.org/10.1002/2014JB011547

Authors and Affiliations

Viviana Wöhnke[1] · Annette Eicker[1] · Matthias Weigelt[2,3] · Marvin Reich[4] · Andreas Güntner[4,5] · Andreas Kvas[6] · Torsten Mayer-Gürr[7]

✉ Viviana Wöhnke
viviana.woehnke@hcu-hamburg.de

Annette Eicker
annette.eicker@hcu-hamburg.de

Matthias Weigelt
matthias.weigelt@dlr.de

Marvin Reich
mreich@gfz-potsdam.de

Andreas Güntner
andreas.guentner@gfz-potsdam.de

Andreas Kvas
andreas.kvas@uni-graz.at

Torsten Mayer-Gürr
mayer-guerr@tugraz.at

1 Geodesy and Geoinformatics, HafenCity University Hamburg, Henning-Voscherau-Platz 1, Hamburg 20457, Hamburg, Germany

2 Institute for Satellite Geodesy and Inertial Sensing, German Aerospace Center (DLR), Callinstraße 30b, Hannover 30167, Lower Saxony, Germany

3 Institute of Geodesy, Leibniz University Hannover, Schneiderberg 50, Hannover 30167, Lower Saxony, Germany

4 Helmholtz Centre Potsdam - GFZ German Research Centre for Geosciences, Telegrafenberg, Potsdam 14473, Brandenburg, Germany

5 Institute of Environmental Science and Geography, University of Potsdam, Karl-Liebknecht-Strasse 24-25, Potsdam 14476, Brandenburg, Germany

6 Wegener Center for Climate and Global Change, University of Graz, Brandhofgasse 5, Graz 8010, Styria, Austria

7 Institute of Geodesy, Graz University of Technology, Steyrergasse 30/III, Graz 8010, Styria, Austria